Optical second-harmonic generation induced by electric current in graphene on Si and SiC substrates

Yong Q. An,[1,*] J. E. Rowe,[2] Daniel B. Dougherty,[2] Ji Ung Lee,[1] and Alain C. Diebold[1]
[1]*College of Nanoscale Science and Engineering, State University of New York, Albany, New York 12203, USA*
[2]*Department of Physics, North Carolina State University, Raleigh, North Carolina 27695, USA*
(Received 9 December 2013; revised manuscript received 24 February 2014; published 12 March 2014)

We find that the flow of direct electric current (dc) through graphene on substrate enhances surface optical second-harmonic generation (SHG) from the graphene/substrate system. The current can enhance surface SHG by about 300% for a chemical-vapor-deposition (CVD) graphene monolayer on a SiO_2/Si(001) substrate, and by about 25% for an epitaxial four-layer-graphene film on a 3.5°-miscut vicinal SiC(0001) substrate. The enhancement in both the CVD and epitaxial graphene samples is due to electric field-induced SHG, which is produced by the current-associated vertical electric field at the SiO_2/Si interface or at the graphene/SiC interface. Measurements of rotational-anisotropy SHG (RA-SH) from both samples revealed that the current-induced SHG varies strongly with the measurement location along the current flow direction. By measuring RA-SH from the vicinal SiC(0001) substrate, we determined all three second-order susceptibility tensor elements ($d_{33} = -52.0$ pm/V, $d_{15} = 20.0$ pm/V, and $d_{31} = 18.7$ pm/V) that characterize the SHG response of hexagonal SiC at the fundamental wavelength of 740 nm. We further determined the three effective susceptibility tensor elements ($d_{33} = -135.8$ pm/V, $d_{15} = 18.5$ pm/V, and $d_{31} = 14.6$ pm/V) that characterize the surface SHG from the graphene/vicinal-SiC(0001) sample and finally showed that the current-dependent tensor element d_{33} can be enhanced to a large value of $d_{33} = -199.0$ pm/V by electric current in epitaxial graphene.

DOI: 10.1103/PhysRevB.89.115310 PACS number(s): 78.67.Wj, 78.20.Jq, 78.47.jh, 42.65.Ky

I. INTRODUCTION

Graphene is a monolayer of carbon atoms arranged in a honeycomb lattice. Its two-dimensional hexagonal crystal structure leads to unique material properties, such as a zero-gap Dirac-cone band structure, massless Dirac fermion carriers, and high mobility of these carriers [1–3]. These superior electronic and transport properties may give rise to potential applications in future nanoelectronic devices. The linear optical and ultrafast optical properties of graphene have been intensively studied to correlate the material properties to the Dirac-cone band structure and cone-related carrier dynamics [4–9]. In contrast, the nonlinear optical properties of graphene [10–14] have been studied to a lesser extent due to its weak nonlinear optical response. Recently, theoretical calculations have shown that graphene can be a nonlinear optical material with giant nonlinearity when it is electrically biased or optically excited [15,16]. The second-order nonlinear susceptibility $\chi^{(2)}$ has been predicted to be enhanced by several orders of magnitude when an electric current is applied to bilayer graphene [15] or when surface plasmons are excited in single-layer graphene [16]. Experimental verification of the predicted giant optical nonlinearity is an important step toward implementing the effect in optical devices. Field-effect transistors (FET) with graphene channels [17,18] are suitable structures for the study of such electro-optical effects, not only because the graphene film in the channel region can be easily biased by either an electric current or field, but also because the optical transparency of graphene facilitates our nonlinear optical measurements. Nonlinear optical studies of graphene FET channels will elucidate new opportunities for combining high electron mobility with giant optical nonlinearity resulting in new optoelectronic devices.

Optical second-harmonic generation (SHG), a simple but important second-order nonlinear optical process, is forbidden in a freestanding graphene monolayer because of the centrosymmetry of the graphene's crystal structure [19–22]. However, SHG from a graphene/substrate system becomes allowed, in principle, because the substrate may break the symmetry of the system. Accordingly, surface SHG from exfoliated graphene on a SiO_2/Si(001) substrate was recently observed by examining the interference patterns formed by two SHG contributions, one from graphene and the other from the underlying SiO_2/Si(001) substrate [23,24]. The symmetry of the graphene/substrate system may also be broken by an electric current or field in graphene, resulting in current or field-induced SHG [25]. It was recently reported that a direct electric current (dc) in multilayer graphene that is supported by a SiO_2/Si(001) substrate could enhance surface SHG [26] by nearly 30% when the current was applied into graphene through a pair of needle electrodes. Although electric current-induced SHG (CI-SH) [27] has been observed in other semiconductor materials, such as silicon [28] and GaAs [29], observation of CI-SH in graphene is particularly remarkable because confining the electric current in a single layer or a few atomic layers allows one to directly infer the mechanism of CI-SH effects.

For SH or CI-SH measurements, it is desirable to use graphene sheets of large areas because the focused laser spot for SHG is often as large as tens of micrometers and thus requires a larger graphene area to accommodate the beam spot. Moreover, it is desirable to scan the laser spot on a graphene area with an adequate range of displacement for accurately comparing SH signals at different measurement locations. Defect-free single-crystal graphene samples, such as the flakes produced by the "scotch tape" method (mechanical

*yan2@albany.edu

exfoliation from bulk graphite), are usually as small as several micrometers, and it is difficult to scan the laser beam on one particular flake. Polycrystalline or epitaxial single-crystal graphene samples, however, can easily be produced by growing millimeter-sized graphene films, which are large enough for scanning SHG to move the laser spot both laterally and rotationally. Currently, there are mainly two growth methods to produce large-area crystalline graphene films: one is the chemical vapor deposition (CVD) of graphene onto metallic foils, and the other is the epitaxial growth of single-crystal graphene on single-crystal surfaces of silicon carbide (SiC). Here, we study the CI-SH effect from large-area graphene films produced from both growth methods. The CVD graphene film in this work was first grown on a copper foil and then transferred onto a SiO_2/Si(001) substrate, resulting in a graphene/SiO_2/Si(001) sample. The epitaxial graphene was grown directly on the vicinal (0001) surface of a 6*H* hexagonal SiC substrate by thermal annealing the substrate in vacuum, which left a carbon layer on SiC, producing a graphene/vicinal-SiC(0001) sample.

The SH signal in reflection from these graphene/substrate samples may include both a bulk SH contribution from the supporting substrate and a surface SH contribution from the graphene film and the interfaces underneath the film. Meanwhile, the CI-SH effect from the system may be always accompanied by the electric field-induced SHG (FI-SH) effect, because the electric current in graphene is applied through an external electric field, and thus they are inseparable. The entanglement of the two SH contributions along with the two electro-optic effects makes it difficult to identify which contribution or effect is the primary factor responsible for enhancement of SHG. Rotational-anisotropy SHG (RA-SH) is a convenient technique for disentangling different sources of SHG from the graphene/substrate system. In a typical RA-SH scan, the SH signal varies with the sample azimuthal angle because the SHG from the surface or graphene and that from the substrate interfere constructively or destructively depending on the sample orientation with respect to the laser beams. The surface SH contribution from graphene is isotropic, while the bulk SH contributions from the crystalline substrates, such as Si(001) and vicinal SiC(0001), are anisotropic. The interference of the isotropic and the anisotropic SH contributions results in modulation of SHG with the sample azimuthal angle. The interference may amplify the overall SH intensity and thus increase detection sensitivity, and it also provides the information for determining both the amplitude and the phase of the SH field.

Here, we present a comprehensive study of the CI-SH effect from two graphene/substrate samples: a CVD polycrystalline graphene/SiO_2/Si(001) sample and an epitaxial single-crystal graphene/vicinal-SiC(0001) sample. Although we recently reported the experimental results of CI-SH from the graphene/SiO_2/Si(001) sample in a Letter [30], here we review those results and contrast them to our new experimental results of CI-SH from the graphene/vicinal-SiC(0001) sample. We also provide additional information concerning previous measurements. Here, the SH signals from the two samples are normalized in the same way and thus are directly comparable to each other. We consistently find for both samples that the CI-SH signal in the reflection configuration from current-biased graphene varies strongly with the measurement location along the current flow direction. However, we find that the traces of variation of SHG with the measurement location appear different for the two samples. Section II of this paper describes the sample preparation, the laser system, and the SH detection system in detail. Section III A describes the experimental results of CI-SH from the graphene/SiO_2/Si(001) sample and the phenomenological theory of RA-SH for the mechanism of CI-SH. Section III B describes the experimental results of CI-SH from the graphene/vicinal-SiC(0001) sample and the phenomenological theory of RA-SH and CI-SH. In this section, we also demonstrate that measurements of RA-SH from the vicinal SiC(0001) substrate allow for determination of the second-order susceptibility tensor elements of SiC. Furthermore, we discuss the similarities and differences between the CI-SH effects observed from the two samples. Section IV summarizes the conclusions from the CI-SH studies of both samples.

II. EXPERIMENT

A. CVD graphene growth and electrode patterning

The CVD graphene was grown on a copper (Cu) foil by chemical vapor deposition using a combined flow of hydrogen and methane and then transferred onto a SiO_2/Si(001) substrate by a polymethyl methacrylate (PMMA)-based method using common procedures as described elsewhere [31,32]. The SiO_2 layer of the Si substrate was 300 nm thick. Decomposition of the flowing methane onto the Cu foil results from a surface catalyzed reaction that leaves predominantly monolayer graphene due to carbon's insolubility in Cu. Graphene produced from this procedure is polycrystalline and consists of domain sizes on the order of several microns. The domain (grain) size of the graphene film was found from dark-field transmission electron microscopy. The presence of monolayer graphene was verified using Raman spectroscopy. The graphene monolayer covered a $\sim 10 \times 10\text{-mm}^2$ surface area on the SiO_2/Si(001) substrate.

On top of the CVD graphene/SiO_2/Si(001) sample, we patterned a pair of parallel copper electrodes, separated by a 1.3-mm gap and aligned in the Si[110] direction (which lies in the mirror plane of symmetry in Si), through which electric current is applied into graphene. In order to study the current-associated FI-SH effect in the sample, we also deposited a third electrode on the back of the heavily doped Si substrate for applying a dc bias voltage across the SiO_2/Si interface. These three electrodes resemble the source (S), drain (D), and gate (G) terminals of an FET structure, but here the graphene channel is large, allowing RA-SH measurements at different channel locations.

B. Epitaxial graphene growth and electrode patterning

The epitaxial graphene was grown directly on a crystalline SiC substrate by the vacuum annealing of SiC at high temperatures [33,34]. The substrate SiC is a promising material for microelectronic and optoelectronic applications, especially in high-power devices because of its high breakdown electric field. Its endurance to high temperatures and its wide electronic bandgap also make SiC attractive for nonlinear optical

applications, such as frequency conversion of high-power laser in a wide spectral range. Among the ~250 crystalline structures (polytypes) that have been identified for the material SiC, the hexagonal polytype 6*H* is the most commonly encountered one.

The growth results from the sublimation of Si from the step edges of the SiC terraces at the surface. In order to have a high density of step edges on the sample surface to facilitate the Si sublimation, vicinal 6*H*-SiC(0001) substrates with a miscut angle of 3.5° tilting from the [0001] direction toward the [11$\bar{2}$0] direction were used for the epitaxial growth of graphene on SiC. During annealing, there is step bunching of single-layer steps into triple-layer steps that are covered with single, double, and triple layers of graphene. This was measured using scanning tunneling microscope (STM) at room temperature with a final thickness averaging ~4 layers of graphene as determined by the attenuation of the Si-LVV Auger transition relative to the C-KVV Auger transition. The initial substrates were oriented with the Si-terminated face and then cleaned by chemical-mechanical polishing (CMP) and hydrofluoric acid (HF) etching. After this procedure, they were annealed at about 900 °C prior to growth in order to remove the native oxide. The graphene growth was performed in ultrahigh vacuum at about 1400 °C for approximately 3 min. The growth technique produced a four-layer-graphene film with a Bernal stacking arrangement [33,34], and the thickness was determined by *in situ* STM and confirmed by Auger methods. The surface area of the graphene film was $3 \times 9\,\text{mm}^2$, completely covering the front surface of the vicinal SiC(0001) substrate. To prevent the multiple-reflection effects inside the sample slab, the back surface of the SiC substrate was mechanically roughed by sandblasting prior to chemical cleaning and graphene growth. The sample was examined and found to be quite uniform due to the heating by direct current through the SiC substrate with temperature uniform over the ~3-mm area within ~30 °C or better, limited by our optical pyrometer precision.

On top of the epitaxial graphene/vicinal-SiC(0001) sample, we patterned a pair of parallel copper electrodes, separated by a 2-mm gap and aligned perpendicular to the [11$\bar{2}$0] direction of the SiC crystal, through which electric current is applied into graphene. With this geometry of the system, the current flow direction in graphene is always perpendicular to the step edges of miscut in the vicinal surface, and the current flow direction always lies in a mirror plane of symmetry of SiC. These two electrodes are designated as the source (S) and drain (D) to analogize them to the top terminals of an FET structure.

C. Laser and detection system

Second-harmonic generation measurements used laser pulses of 120 fs duration at a repetition rate of 82 MHz produced from a Ti:sapphire laser. The laser beam was focused to a 30-μm spot on the sample at an incident angle of 45°. The peak intensity of the laser beam was 2.1 GW/cm^2. The laser fluence was 260 μJ/cm^2 per pulse, which was far below the damage threshold of graphene, reportedly at the level of at least tens of millijoules per square centimeter per pulse. The SH signal in reflection from the sample surface was measured in air at room temperature by a photomultiplier tube (PMT). The sample was mounted on a rotation stage for rotational-anisotropy SHG (RA-SH) measurements, producing SH signals varying with the sample azimuthal angle ϕ. Both *p* and *s* polarizations were used for either the incident beam or the SH analyzer to separate different SH components. The *pp* polarization represents the *p*-polarized fundamental and *p*-polarized SH configuration, etc. The fundamental wavelength was fixed at 740 nm to match the E_1 critical point transition in Si, so that the interference between the isotropic SHG from graphene and the anisotropic SHG from the Si(001) substrate is the strongest [35,36].

For the detection of the SH signal, a set of color glass filters were placed in the optical path before the PMT to select the wavelength in the vicinity of the SH light. A bandpass filter with a 10-nm bandwidth was used to verify whether the detected light was at the SH wavelength. Special care was taken to ensure that the photoluminescence light [9] from graphene that is excited by the laser pulses was not significantly mixed into the SH signal. In the experiment, the solid angle for collecting photoluminescence was small ($<\pi/64$), and a spatial filter (iris) in the beam path was able to control the amount of photoluminescence light into the PMT. The added PMT signal due to the photoluminescence from graphene was found to be negligible.

III. RESULTS AND DISCUSSION

A. SHG from graphene/SiO$_2$/Si(001)

The incident laser beam at frequency ω generates a source of polarization in the medium at the SH frequency 2ω, which radiates the SH light for the measurement. The second-order susceptibility tensor $\chi^{(2)}_{ijk}$ can be introduced to connect the fundamental field $E^{(\omega)}_i$ and the generated SH field $E^{(2\omega)}_i$, where each subscript i, j, and k can be replaced by x, y, or z to represent the three crystallographic coordinates [100], [010], and [001], respectively. The SH polarization $P^{(2\omega)}_i$ in the medium is given by

$$P^{(2\omega)}_i = \varepsilon_0 \chi^{(2)}_{ijk} E^{(\omega)}_j E^{(\omega)}_k, \tag{1}$$

where ε_0 is the permittivity of vacuum, and summation applies over the repeated indices. The resulting SH intensity is proportional to the square of the absolute value of the SH field $E^{(2\omega)}_i$, while $E^{(2\omega)}_i$ is proportional to the SH polarization $P^{(2\omega)}_i$ in Eq. (1). The 27 tensor elements of $\chi^{(2)}_{ijk}$ are often not independent, and for a crystalline medium in the natural crystallographic coordinates, most of these tensor elements become zero because of symmetry. These nonzero tensor elements are treated as the sources of the SH polarization.

The rotational-anisotropy SHG (RA-SH pattern) can be predicted by transforming the susceptibility tensor from the crystallographic coordinates to the beam coordinates using a transformation matrix. For the sample rotation counterclockwise about the z axis by an angle ϕ, the corresponding transformation matrix is

$$R(\phi) = \begin{bmatrix} \cos(\phi) & \sin(\phi) & 0 \\ -\sin(\phi) & \cos(\phi) & 0 \\ 0 & 0 & 1 \end{bmatrix}. \tag{2}$$

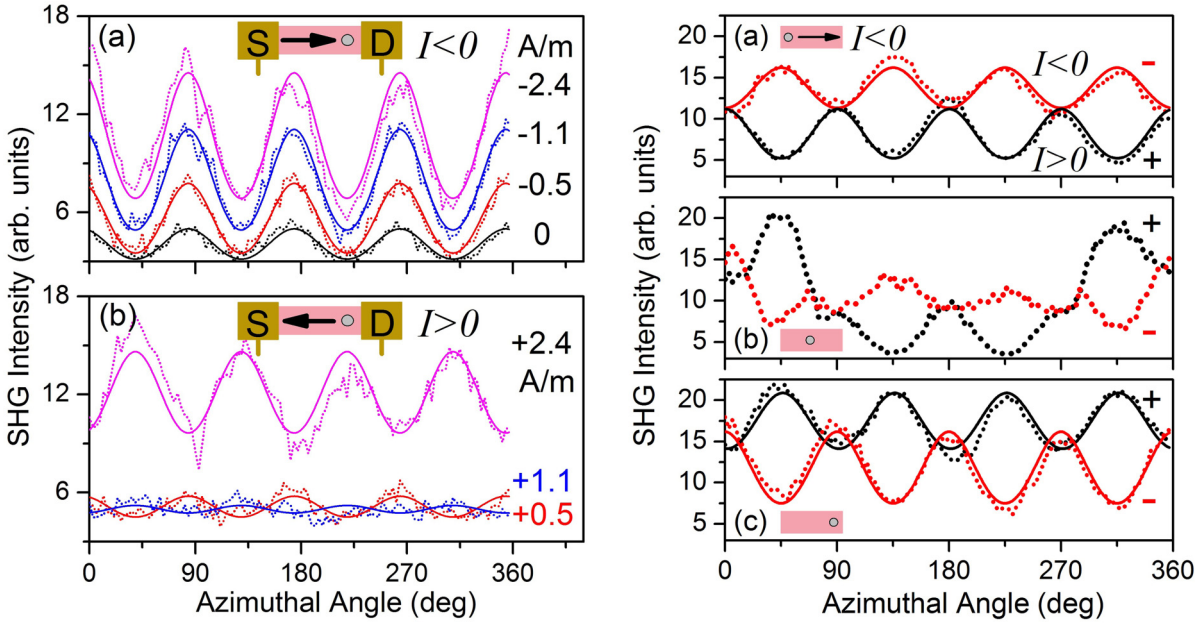

FIG. 1. (Color online) (a), (left panel): Measured rotational-anisotropy SHG (RA-SH) scans from the graphene/SiO_2/Si(001) sample at a fixed graphene location for 0 and different negative currents (−0.5, −1.1, and −2.4 A/m). (b), (left panel): The above scans for different positive currents. The S and D electrodes, measurement location, and definition of the negative/positive current direction are illustrated by the inset in each panel. Right panel: RA-SH scans at a fixed current $I = \pm 2.4$ A/m measured at three different graphene locations: (a) nearby the S electrode, (b) halfway between S and D, and (c) nearby the D electrode. Measurement locations are illustrated in each panel as an inset.

The tensor in the crystallographic coordinate $\chi^{(2)}_{ijk}$ is transformed to that in the beam coordinate $\chi^{(2),b}_{lmn}$ according to the tensor transformation rule

$$\chi^{(2),b}_{lmn}(\phi) = R_{li}(\phi)R_{mj}(\phi)R_{nk}(\phi)\chi^{(2)}_{ijk}, \tag{3}$$

where summation applies over repeated indices, and $R_{nk}(\phi)$ indicates the nk element of the matrix in Eq. (2). This rotational transformation usually introduces onefold, twofold, and threefold anisotropic SH terms in the forms $\cos(n\phi)$ and $\sin(n\phi)$, where $n = 1$, 2, or 3, in addition to an isotropic SH term.

For the graphene/SiO_2/Si(001) sample, there are two possible SH sources of the dipole response: the graphene film and the SiO_2/Si interface, due to the SH polarization sheets at the surface or interface. The Si(001) surface has a fourfold rotation axis around the surface normal, and thus its susceptibility tensor has only three independent nonzero tensor elements $\chi^{(2)}_{zxx} = \chi^{(2)}_{zyy}$, $\chi^{(2)}_{xxz} = \chi^{(2)}_{yyz}$, and $\chi^{(2)}_{zzz}$. For simplicity, we use the piezoelectric contracted notation to replace the three nonzero elements as follows:

$$d_{31} = \chi^{(2)}_{zxx}, \quad d_{15} = \chi^{(2)}_{xxz}, \quad \text{and} \quad d_{33} = \chi^{(2)}_{zzz}. \tag{4}$$

A single-crystal graphene monolayer has a sixfold rotation axis around the surface normal, giving it higher symmetry than Si(001), and thus its susceptibility tensor has the same structure of elements as that of the Si(001) surface, i.e. graphene has only three nonzero elements d_{31}, d_{15}, and d_{33}. The rotational transformation, as described by Eq. (3), of such a highly symmetric tensor yields an invariant tensor, i.e. $\chi^{(2),b}_{lmn}(\phi) = \chi^{(2)}_{ijk}$. This means that the new tensor in the beam coordinates is independent of the rotation angle ϕ. Therefore, the SH components from both the graphene film and the SiO_2/Si interface are isotropic.

Although there is no SH polarization through the dipole response in the bulk of Si or SiO_2, i.e. $\chi^{(2)}_{ijk} = 0$ because of centrosymmetry, there is still a nonzero source of SH polarization through higher-order terms, such as the electric quadrupole response. For Si, the quadrupole SH response in the bulk is usually much weaker than the dipole SH response at the surface, but it can be quite significant when constructively interfering with the surface dipole SH response. The bulk quadrupole SH polarization can be described by a third-order susceptibility tensor $\chi^{(3)}_{ijkl}$ to connect the fundamental field and the generated SH field [37,38]. For the sample rotation about the z axis by an angle ϕ, the tensor in the crystallographic coordinate $\chi^{(3)}_{ijkl}$ is transformed to that in the beam coordinate $\chi^{(3),b}_{opqr}$ according to the tensor transformation rule

$$\chi^{(3),b}_{opqr}(\phi) = R_{oi}(\phi)R_{pj}(\phi)R_{qk}(\phi)R_{rl}(\phi)\chi^{(3)}_{ijkl}. \tag{5}$$

For SHG from the Si(001) face, this rotational transformation introduces only fourfold anisotropic SH terms in the forms of $\cos(4\phi)$ and $\sin(4\phi)$, in addition to an isotropic SH term. Therefore, any fourfold rotational anisotropy of SHG from the graphene/SiO_2/Si(001) sample can be entirely attributed to the bulk quadrupole SH contribution from the Si substrate.

Figure 1(a), (left panel), shows the RA-SH signals measured at a fixed graphene location near (0.3 mm from) the D electrode for 0 and different negative currents (−0.5, −1.1, and −2.4 A/m), and Fig. 1(b), (left panel), shows those RA-SH signals measured at the same graphene location for different positive currents. Here, negative current is defined as the current that flows from S to D, as indicated by the inset of Fig. 1(a), (left panel). All currents are normalized by the width

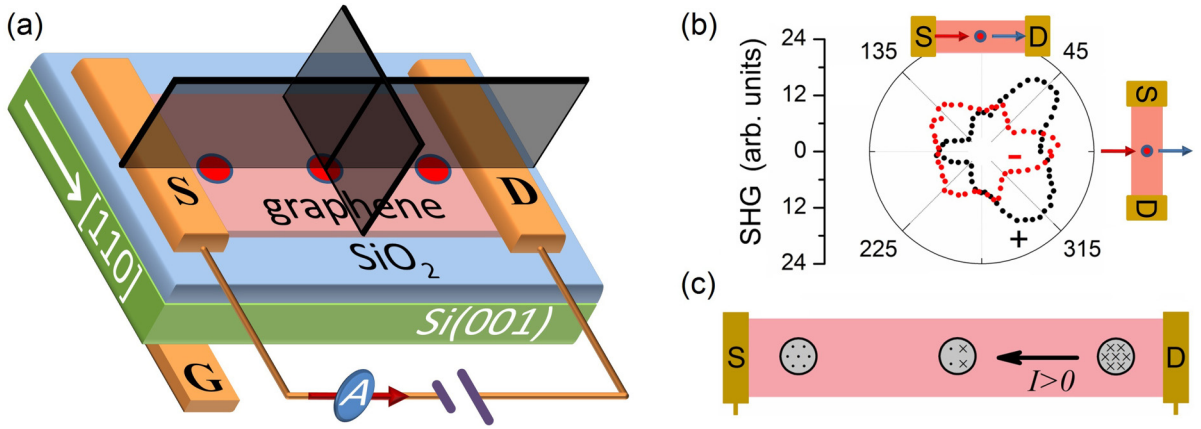

FIG. 2. (Color online) (a) Schematic illustration of the graphene/SiO_2/Si(001) sample with patterned electrodes, showing two mirror planes of symmetry of the system when $I = 0$. (b) Polar plot of RA-SH scans measured at the central graphene location for a fixed current of ± 2.4 A/m, showing kitelike RA-SH patterns. Electric current is in (perpendicular to) the plane of incidence when $\phi = 90°$ (0°), as illustrated by the insets. (c) Schematic illustration of the lateral distribution of local electric field across the SiO_2/Si interface, laser sampling ring, definition of the positive ($I > 0$) current direction.

of the current-biased graphene and listed in amperes per meter (A/m). At the maximum current amplitude, the observed SH signal is enhanced about three times by the current in graphene. All RA-SH scans show fourfold symmetry because of the cubic symmetry of the Si(001) lattice. The hexagonal lattice of graphene will only produce an isotropic SH component, and moreover, randomly oriented small graphene domains inside the relatively large beam spot further ensure that any SHG contribution from graphene is isotropic. The *pp*-polarized RA-SH intensity at 2ω frequency from the graphene/SiO_2/Si(001) sample takes the form [24,35]

$$I_{pp}^{(2\omega)}(\phi) = [a_0 + a_4 \cos(4\phi)]^2, \tag{6}$$

where the coefficients a_0 and a_4 are the amplitudes of the isotropic and anisotropic terms, respectively, and ϕ is the sample azimuthal angle between the incident plane and the [110] direction in the Si(001) surface. Note that a_4 arises entirely from the fourfold rotational symmetry of the Si(001) bulk.

When current flows in graphene, a_0 in Eq. (6) may be split into three terms [38,39],

$$a_0 = a_0^{Si} + a_0^C + \sum_{n=0}^{3} a_n^I I \cos[n(\phi + 90°)]. \tag{7}$$

Here, a_0^{Si} comes from SHG at the SiO_2/Si interface, a_0^C is due to SHG from graphene when $I = 0$, and a_n^I is due to CI-SH in graphene, where $n = 0$, 1, 2, or 3. Comparison of the measured RA-SH scans from bare and graphene covered SiO_2/Si(001) surfaces shows that the SH contribution from graphene alone is negligible, i.e. $a_0^C = 0$. This means that the second-order susceptibility $\chi^{(2)} = 0$ for graphene, even on a supporting substrate. However, strong third-harmonic generation has recently been observed on a graphene/glass sample [14], suggesting a large third-order susceptibility $\chi^{(3)}$ for graphene. All RA-SH patterns in Fig. 1 (left panel) appear fourfold symmetric, indicating that the observed CI-SH is isotropic with respect to the sample orientation, i.e. a_1^I, a_2^I, and $a_3^I = 0$ in Eq. (7).

We find that the observed RA-SH pattern from the graphene/SiO_2/Si(001) sample varies strongly with the measurement location, as shown in Fig. 1 (right panel). For a fixed current direction, the RA-SH pattern undergoes a phase inversion as the measurement location is shifted along the current flow direction. The peaks of the RA-SH scan are turned into valleys as the measurement location is shifted from the (a) current upstream to (b) midstream to (c) downstream region. The result means that CI-SH is not a simple function of current, but rather a function of the local electric field. This also means that the current-dependent term $a_0^I = 0$ in Eq. (7). Figure 1(b), (right panel), shows onefold symmetric RA-SH scans each with five peaks in the central graphene region; however, the onefold symmetry is not predicted by Eq. (6).

These unusual onefold RA-SH scans seemingly are predicted by the current term in Eq. (7), but symmetry consideration of RA-SH also shows otherwise. As shown in Fig. 2(a), both the [110] and [1$\bar{1}$0] directions are in a mirror plane of symmetry of the electrode/graphene/SiO_2/Si(001) system when $I = 0$. However, the [110] direction in Fig. 2(a) is no longer in a mirror plane of symmetry of the system when $I \neq 0$ because current flow in graphene breaks the mirror symmetry. Figure 2(b) shows the polar plot of the measured RA-SH pattern [from the same data in Fig. 1(b), (right panel)] in the central region of graphene between the S and D electrodes. The two patterns show a mirror plane of symmetry along the $\phi = 0$ direction, which is, however, off by 90° from the predicted direction from Eq. (7).

The appearance of the mirror plane of symmetry along the $\phi = 0$ direction in Fig. 2(b) can be explained by the lateral distribution of the vertical electric field along the current flow direction, while the field produces FI-SH at the SiO_2/Si interface [40]. When a RA-SH scan is measured, the laser spot does not sit on a fixed sample spot, but actually traces a tiny ring on the sample surface when the sample is rotated 360°. This trace forms a laser sampling ring on graphene,

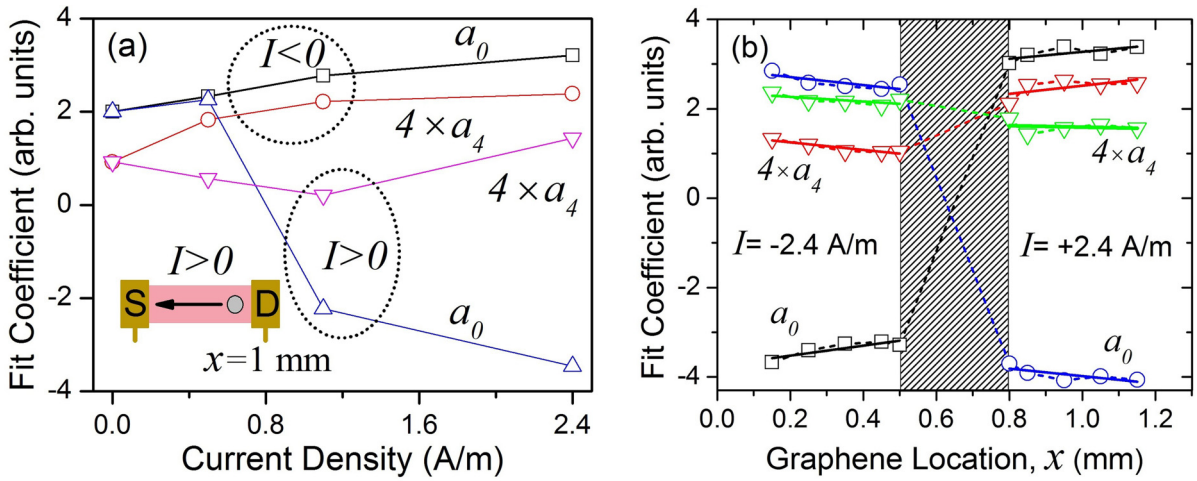

FIG. 3. (Color online) (a) Fit coefficients a_0 and $4 \times a_4$ of RA-SH patterns in Fig. 1 (left panel) measured at a fixed graphene location $x = 1.00$ mm for different current amplitudes and both positive and negative current directions. The measurement location with respect to the S and D electrodes and the positive current direction are illustrated by the inset. (b) Fit coefficients a_0 and $4 \times a_4$ at different graphene locations x, at a fixed current amplitude $I = 2.4$ A/m, and for both positive and negative current directions. Note that a sign flip of a_0 develops through a 0.3-mm-wide transition region in the central graphene area.

as schematically plotted in Fig. 2(c), which is caused mainly by the nonideal alignment of the laser beam off the sample rotation axis and slightly by the mechanical wobbling of the rotation stage. The diameter of the laser sampling ring in our experiments was 0.1 mm, setting a spatial resolution of our RA-SH measurements as 0.1 mm. For the positive current in Fig. 2(c), we can assume that there is a vertical electrical field pointing upward on the S-electrode side but downward on the D-electrode side. The field is uniformly distributed in the region close to either electrode but varies abruptly from the upward to the downward direction in the central transition region. When the laser sampling ring rides over the transition region, a half of the RA-SH scan measures the upward field, and the other half measures the downward field. This situation will result in a onefold symmetric RA-SH scan that is distorted from a fourfold symmetric one. The vertical electrical field can be introduced by two sources: the externally applied field on graphene and the induced field by the trapped charges at the graphene/SiO_2 interface.

Figure 3(a) shows the Eq. (6) fit coefficients a_0 and a_4 of the RA-SH scans in Fig. 1 (left panel) for different current values and directions. All these RA-SH scans were measured at the same graphene location $x = 1.00$ mm. Here, x is defined as the distance measured from S to D. For the negative current, a_0 increases almost linearly with current. For the positive current, however, a_0 crosses zero at $I = 0.7$ A/m and then linearly increases in magnitude. Reversing the current direction at a fixed graphene location can introduce a sign change of a_0. The slight variation of a_4 with the current amplitude or direction suggests that the current in graphene likely affects the SH response in the Si(001) substrate.

Figure 3(b) shows the Eq. (6) fit coefficients a_0 and a_4 of the RA-SH scans as a function of the graphene location x for a fixed current of ± 2.4 A/m. Within 0.5 mm from either S or D, the RA-SH scans appear fourfold symmetric and thus can be fit to Eq. (6). Approximately midway between S and D, the RA-SH scans gradually distort to be onefold symmetric, with the maximum distortion occurring at the middle location $x = 0.65$ mm, as shown in Fig. 2(b). The transition region for completing a phase inversion is found to be about 0.3 mm wide. The spatial resolution for determining the transition width is limited by the diameter of the laser sampling ring, which is 0.1 mm in the experiment. The onefold symmetric RA-SH scans in the transition region cannot be simply fit to fourfold symmetric Eq. (6).

As current flows in graphene, a potential difference exists between graphene and the underneath Si substrate, resulting in a vertical electric field E, and thus a FI-SH effect across the SiO_2/Si interface [40]. The FI-SH itself can be independently studied by applying a dc bias voltage between the S (or D) and G electrodes without applying a current in graphene. The *pp*-polarized RA-SH signals in reflection from a measurement location midway between the S and D electrodes of the graphene/SiO_2/Si(001) sample for zero and the positive bias voltages (0, 6, 12, 18, and 25 V) are shown in Fig. 4(a), and those for zero and the negative bias voltages are shown in Fig. 4(b). Here, positive bias is defined as bias with a higher voltage on S than G. The RA-SH scans measured at different locations between the S and D appear about the same in amplitude and consistently the same in phase. Figures 4(a) and 4(b) show that switching the bias polarity can cause a phase inversion of SHG, similar to that of CI-SH.

If an electric field E is present across the SiO_2/Si interface, a_0 in Eq. (6) may be split into two terms

$$a_0 = a_0^{Si} + a_0^E E. \tag{8}$$

Here, a_0^{Si} has the same interpretation as in Eq. (7), and a_0^E arises from the FI-SH at the SiO_2/Si interface. The bias field E is proportional to the bias voltage, while the surface charge (electron) density on graphene is proportional to E. Figure 4(c) shows the Eq. (6) fit coefficients a_0 and a_4 of the RA-SH scans at different bias voltages. For either bias polarity, a_0 increases linearly with the bias magnitude above 6 V, following the prediction of Eq. (8). For positive bias,

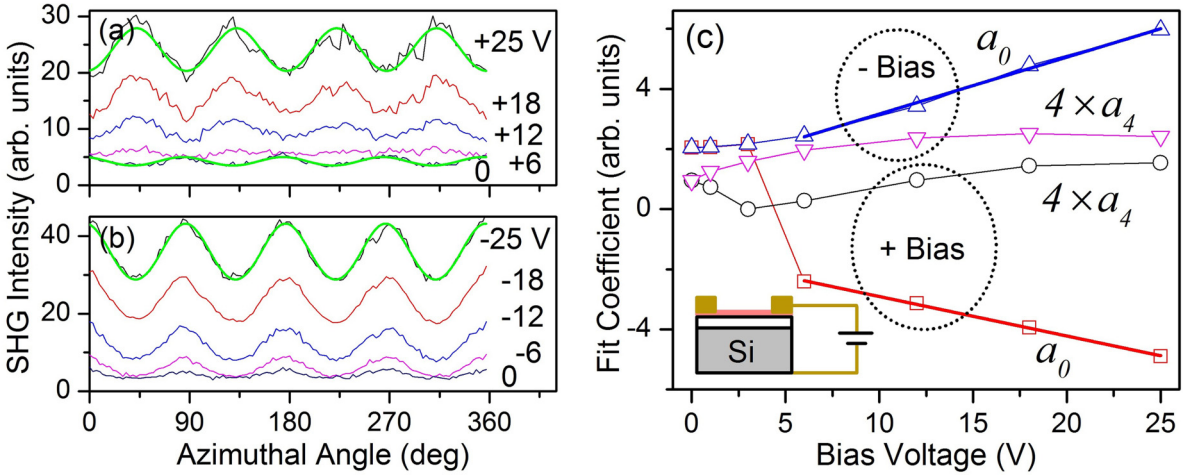

FIG. 4. (Color online) (a) Measured rotational-anisotropy SHG (RA-SH) scans from the graphene/SiO_2/Si(001) sample for zero and different positive bias voltages (+6, +12, +18, and +25 V). (b) The above RA-SH scans for zero and different negative bias voltages. Thin lines in (a) and (b) are experimental data, and thick smooth curves are Eq. (6) fits. (c) Fit coefficients a_0 and $4 \times a_4$ for different bias voltages and polarities. Linear fits of the bias-dependence of a_0 are shown for bias amplitudes above 6 V. The positive bias situation for the measurement of electric field-induced SHG (FI-SH) is illustrated by the inset.

however, a_0 crosses zero at a bias of 5 V. The FI-SH in Fig. 4 resembles the CI-SH in Fig. 1 (left panel) in two respects: the polarity-correlated phase inversion and the voltage dependence of a_0. In the FI-SH measurements, the graphene monolayer serves as a transparent electrode for application of a vertical bias across the SiO_2/Si interface. However, the observed FI-SH results resemble earlier studies when a chromium layer served as such an electrode [40–42]. Therefore, we attribute the observed CI-SH from the graphene/SiO_2/Si(001) structure to current-associated FI-SH at the SiO_2/Si interface.

As shown in Fig. 3(b), a_4 drops roughly 50% as the graphene location x varies from the downstream to the upstream region of the current. This drop can be understood in terms of charge trapping at the graphene/SiO_2 interface. In the current downstream region, negative charges are trapped at the graphene/SiO_2 interface, repelling near-interface electrons in Si away from the SiO_2/Si interface. Therefore, the space charge region in Si is enlarged and thus a stronger quadrupole SH contribution is generated from the bulk of Si. This explanation is corroborated not only by the FI-SH results in Fig. 4(c), showing a larger a_4 under negative bias than positive bias consistently for all bias voltages, but also by the CI-SH results in Fig. 3(a), showing a larger a_4 when $I < 0$ than $I > 0$ consistently for all current values.

The isotropic coefficient a_0 varies abruptly with x from positive to negative in the narrow transition region, corresponding to polarity switch of the vertical electric field. The downward field in the current upstream region can be formed by the potential drop between graphene and the Si substrate, while this field can be equivalently treated as positive charges at the graphene/SiO_2 interface. The upward field in the current downstream region can be introduced by trapped negative chargers (electrons) at the graphene/SiO_2 interface. In Eq. (8), a_0^{Si} is negligible when E is large, and thus the x-dependent surface density of trapped charges is proportional to $-a_0(x)$. Figure 3(b) shows that the along-current lateral distribution of the trapped charges at the current-biased graphene/SiO_2 interface appears similar to the electron distribution in a p-n junction.

The location-dependent voltage applied through top electrodes should be positive everywhere on graphene regardless of the current direction because the cathode (either S or D) electrode on graphene and the G electrode on Si were all grounded in the CI-SH measurements. Assuming that current-associated FI-SH at the SiO_2/Si interface is fully responsible for the observed CI-SH, we would expect that the CI-SH patterns measured everywhere on graphene has the same phase as the FI-SH patterns independently measured with a positive bias field. In other words, the phase of SHG is expected to stay the same everywhere along the current flow direction because the bias field is always positive (downward). The anode-side RA-SH scans in Fig. 1(b), (left panel), show the same phase as those in Fig. 4(a), but the cathode-side RA-SH scans in Fig. 1(a), (left panel), show the opposite phase, which contradicts the expected behavior. We attribute the opposite phase of SHG on the cathode side to trapped electrons at the graphene/SiO_2 interface [43,44]. These negative charges introduce a negative (upward) bias field at the SiO_2/Si interface to reverse the phase of SHG. Charge trapping is believed to occur at the graphene/SiO_2 interface because of the presence of structural defects, such as domain boundaries in graphene, and morphological imperfections, such as spatial gaps between graphene and SiO_2 [45,46].

B. SHG from graphene/vicinal-SiC(0001)

Unlike the centrosymmetric diamond structure of Si, the hexagonal 6H-SiC has a noncentrosymmetric structure; therefore, SHG due to the electric dipole response is allowed in the bulk of SiC. The surface of SiC may also contribute to SHG; however, the bulk SHG contribution will usually dominate the surface SHG contribution due to the relative size of the volume that is sampled in the bulk versus at the surface. Second-harmonic generation due to the quadrupole response

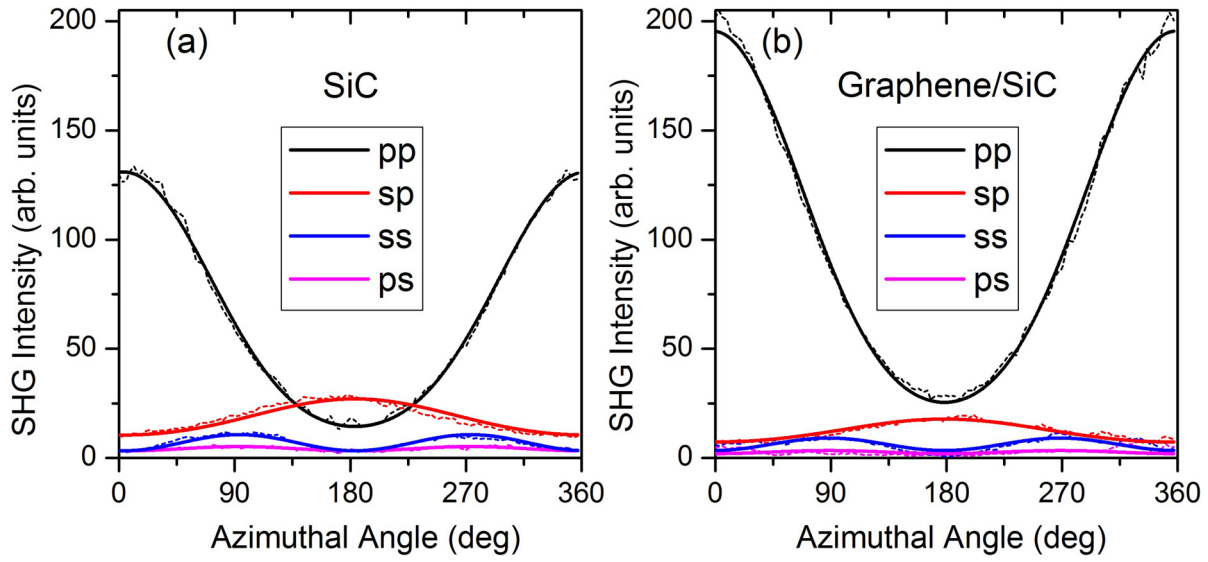

FIG. 5. (Color online) Measured rotational-anisotropy SHG (RA-SH) scans for four different polarization configurations (pp, sp, ss, and ps) from (a) the vicinal SiC(0001) substrate and (b) the graphene/vicinal-SiC(0001) sample. The dotted lines are experimental data, and the smooth curves are Eqs. (9) and (10) fits.

in the bulk of SiC should be much weaker than that due to the dipole response. To extract the SHG response of the graphene film on the graphene/vicinal-SiC(0001) sample, it is critical to understand the dipole SHG response of the SiC substrate.

The SHG susceptibility tensor of the 6H-SiC structure has only three independent nonzero elements: d_{33}, d_{15}, and d_{31}, because the crystal structure possesses the point group 6mm. Although they arise from the dipole response in the SiC bulk, they have the same form of indices as those from the dipole response at the Si surface, as shown in Eq. (4). These elements have been previously measured; however, significant discrepancies still exist among the reported results, and the reported SH wavelength was mostly at 532 nm [47–53]. Most previous measurements were performed using the transmission SHG techniques, mainly including the rotational Maker-fringe technique and the translational wedge technique [47–53]. Because of the optical transmission, multiple-reflection effects inside the sample slab had to be carefully considered in order to accurately derive the tensor elements. In addition, the low transmittance of the SHG light, because of high-refractive indices of SiC, often limited the measurable wavelength range, especially in the ultraviolet region. Using the reflection geometry for the SHG measurements of SiC, we can not only avoid the complication from the multiple-reflection effects but also circumvent the limitation of low optical transmittance.

The SHG in reflection from the normal SiC(0001) surface is isotropic, i.e. independent of the sample azimuthal angle, because SHG of the dipole response is not able to resolve the sixfold rotational symmetry. However, SHG in reflection from a vicinal SiC(0001) surface, which is miscut off the principal (0001) face by a small angle, becomes anisotropic, i.e. dependent on the sample azimuthal angle because the sixfold rotation axis [0001] is slightly tilted off the surface normal direction. The epitaxial graphene film on a vicinal SiC(0001) substrate will only produce an isotropic SH component. The pp-polarized RA-SH intensity at 2ω frequency from the graphene/vicinal-SiC(0001) sample takes the form

$$I_{pp}^{(2\omega)}(\phi) = [a_{0,pp} + a_{1,pp}\cos(\phi)]^2, \tag{9}$$

where the coefficients a_0 and a_1 are the amplitudes of the isotropic and anisotropic terms, respectively. Here, ϕ is the sample azimuthal angle between the incident plane and the plane that contains the miscut angle. To be more specific about the starting angle, we define $\phi = 0$ when the incident beam faces towards the downstairs direction of the miscut steps in the vicinal surface. The sp-polarized RA-SH intensity takes the same form as Eq. (9). The ss-polarized RA-SH intensity at 2ω frequency from the graphene/vicinal-SiC(0001) sample takes the form

$$I_{ss}^{(2\omega)}(\phi) = [a_{1,ss}\sin(\phi)]^2. \tag{10}$$

The ps-polarized RA-SH intensity takes the same form as Eq. (10). Strictly speaking, there should be a twofold term a_2 and a threefold term a_3 to appear in both Eqs. (9) and (10), in the same formula as that in the summation term of Eq. (7); however, the small miscut angle of 3.5° in this work guaranties that both the twofold and threefold coefficients a_2 and a_3 are negligible, as compared to the onefold coefficient a_1.

Figure 5(a) shows the measured RA-SH signals for the four different polarization configurations pp, sp, ss, and ps, from the vicinal SiC(0001) substrate, and Fig. 5(b) shows those RA-SH signals from the epitaxial graphene/vicinal-SiC(0001) sample. As shown, the pp-polarized SH signal at the peak is enhanced about 55% by the growth of epitaxial graphene, while the sp-, ss-, and ps-polarized SH signals at the peaks are consistently diminished about 40%. The result means that the growth of epitaxial graphene on SiC introduces a significant amount of modification to surface SHG. The anisotropic coefficients $a_{1,pp}$ in Eq. (9) and $a_{1,ss}$ in Eq. (10) should arise entirely from the SiC substrate, while the isotropic coefficient $a_{0,pp}$ in Eq. (9) may come from both the graphene film and the SiC substrate. With epitaxial graphene on SiC, $a_{0,pp}$ in Eq. (9)

TABLE I. Fit coefficients a_0 and a_1 of the measured RA-SH scans from the vicinal SiC(0001) substrate and those fit coefficients from the graphene/vicinal-SiC(0001) sample for four different polarization configurations: pp, sp, ss, and ps.

Sample	$a_{0,pp}$	$a_{1,pp}$	$a_{0,sp}$	$a_{1,sp}$	$a_{1,ss}$	$a_{1,ps}$
SiC	−7.62	−3.82	4.23	−0.98	2.71	1.40
Graphene/SiC	−9.51	−4.46	3.46	−0.76	2.38	1.20

may be split into three terms

$$a_{0,pp} = a_0^C + a_0^{C/\mathrm{SiC}} + a_0^{\mathrm{SiC}}. \tag{11}$$

Here, a_0^C arises from graphene only, $a_0^{C/\mathrm{SiC}}$ arises from the graphene/SiC interface, and a_0^{SiC} arises from the SiC substrate. The solid smooth curves in Fig. 5 are Eqs. (9) and (10) fits to the data. The good agreement between the fits and the data suggests high quality of the 6H-SiC crystal structure as well as appropriateness of truncating the twofold and threefold terms in the fit Eqs. (9) and (10). We note that the miscut directions (downstairs or upstairs) of the vicinal SiC(0001) can be determined simply by examining the sp-polarized RA-SH scan in Fig. 5(a) without knowing any value among d_{33}, d_{15}, and d_{31}. This RA-SH scan also provides a technique for measuring the miscut angle of vicinal SiC(0001) substrates.

Table I shows the Eqs. (9) and (10) fit coefficients a_0 and a_1 of the measured RA-SH scans from the vicinal SiC(0001) substrate and the graphene/vicinal-SiC(0001) sample for four different polarization configurations pp, sp, ss, and ps. Both a_0 and a_1 are linear functions of the three susceptibility tensor elements d_{31}, d_{15}, and d_{33}, and linear functions of the refractive indices of SiC. The fit coefficients in Table I are proportional to the SH field, while the SH field is proportional to the square root of the measured SH intensity. Therefore, to solve for the fit coefficients from the SH intensity, there is a ± sign ambiguity for each of the four anisotropic fit coefficients a_1 in Table I. For consistency, we choose $a_{1,sp}$ to be negative based on our numerical simulation result that a positive d_{31} gives a negative $a_{1,sp}$ as the multiplication factor before the fundamental field of light when $\phi = 0$. The relative sign between a_1 of different polarizations and the relative sign between a_0 and a_1 of either pp or sp polarization are determined from the same simulation result.

Comparing a_0 and a_1 from the bare SiC substrate and those from the graphene covered SiC, we find that a_1 of all four polarizations are clearly modified by the graphene growth, while Eqs. (9) and (10) predict that all a_1 should not be modified, if we assume that the change of SHG arises entirely from graphene. The result means that the graphene-induced change of SHG arises from the graphene/SiC interface because the SH contribution from the graphene/SiC interface has the same rotational anisotropy as that from the SiC bulk and thus is able to contribute a onefold anisotropic term a_1. With epitaxial graphene on SiC, $a_{1,pp}$ in Eq. (9) may be split into two terms

$$a_{1,pp} = a_1^{C/\mathrm{SiC}} + a_1^{\mathrm{SiC}}. \tag{12}$$

The growth of epitaxial graphene introduces $a_0^{C/\mathrm{SiC}} \neq 0$ and $a_1^{C/\mathrm{SiC}} \neq 0$, while the SH term arising from the epitaxial graphene film can be set as zero, i.e. $a_0^C = 0$. With epitaxial graphene on SiC, $a_{1,sp}$, $a_{1,ss}$, and $a_{1,ps}$ may also be split into two terms, similar to those in Eq. (12).

Figure 6 shows the measured pp-polarized RA-SH scans at three different measurement locations on the graphene/vicinal-SiC(0001) sample: (a) nearby (0.2 mm from) the S electrode, (b) halfway between S and D, and (c) nearby (0.2 mm from) the D electrode. At each measurement location, the three RA-SH scans in each panel correspond to three different current values in graphene: no current ($I = 0$), positive current at

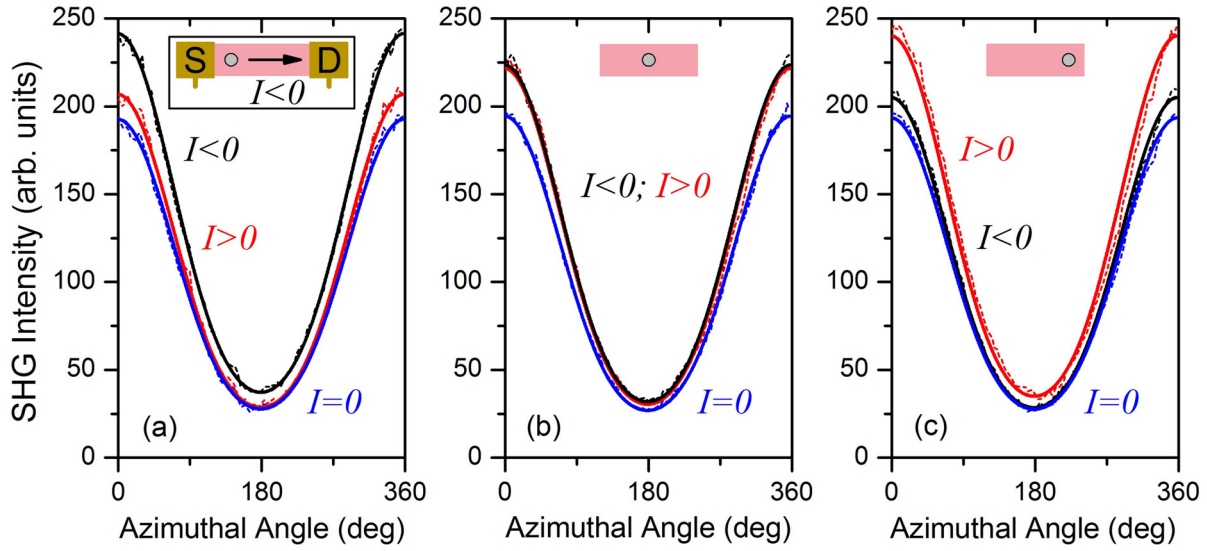

FIG. 6. (Color online) Measured pp-polarized rotational-anisotropy SHG (RA-SH) scans from the graphene/vicinal-SiC(0001) sample when current $I = 0$ and ±23 A/m ($I > 0$ and $I < 0$) in graphene for three different measurement locations (as illustrated by an inset in each panel): (a) nearby the S electrode, (b) halfway between S and D, and (c) nearby the D electrode. The S and D electrodes, measurement location, and definition of the negative current ($I < 0$) are illustrated as an inset in panel (a). The dotted lines are experimental data, and the smooth curves are Eq. (9) fits.

$I = +23$ A/m, and negative current at $I = -23$ A/m. For a fixed current direction, we find that the CI-SH signal increases as the measurement location is shifted from the current downstream to the upstream. The peak SH signal in Fig. 6 is enhanced about 25% by the current flow in graphene. The variation of CI-SH with the measurement location means that the observed CI-SH signal is not solely a function of current. This means that CI-SH in the graphene/vicinal-SiC(0001) sample is not correctly described by the summation term in Eq. (7). The anode-side CI-SH of the positive current is essentially equivalent to the cathode-side CI-SH of the negative current. The result indicates that the location-dependence of CI-SH arises from the current flow, rather than sample nonuniformity. For either current direction, the cathode-side CI-SH signal is only slightly greater than the static SH signal when there is no current in graphene. The result indicates that the observed CI-SH effect arises from the current-associated FI-SH effect at the graphene/SiC interface, where a vertical electric field is accompanied by the current flow. The slight enhancement of the cathode-side CI-SH can be attributed to the close-to-zero vertical electric field there. Note that the cathode electrode on graphene and the SiC substrate were grounded during the CI-SH measurements.

Measurements of the CI-SH effect from the graphene/vicinal-SiC(0001) were also performed for the other three orthogonal polarization configurations sp, ss, and ps, but our results (data of RA-SH scans not shown) indicated that a large current of $I = 23$ A/m in graphene could only introduce a negligible amount of change to the CI-SH signal. In addition, our results of the current dependence of CI-SH (data not shown) indicated that the current-induced change of the peak RA-SH signal for the pp-polarization increases quadratically with the current amplitude.

Table II shows the Eq. (9) fit coefficients $a_{0,pp}$ and $a_{1,pp}$ of the measured RA-SH scans in Fig. 6 at three different measurement locations on the graphene/vicinal-SiC(0001) sample: nearby (0.2 mm from) the S electrode, halfway between S and D, and nearby the D electrode. At each measurement location, a pair of $a_{0,pp}$ and $a_{1,pp}$ are tabulated for three different current values in graphene: no current ($I = 0$), positive current at $I = +23$ A/m, and negative current at $I = -23$ A/m. The minus signs of the two coefficients in Table II are chosen for consistency with the set of signs in Table I. Although both $a_{0,pp}$ and $a_{1,pp}$ in Table II are apparently enhanced by current, the magnitude of enhancement is much less than that by epitaxial growth. With current in epitaxial graphene, the pp-polarized RA-SH intensity at 2ω frequency from the graphene/vicinal-SiC(0001) sample can be written into the form

$$I_{pp}^{(2\omega)}(\phi) = \left[a_0^{C/\mathrm{SiC}} + a_0^{\mathrm{SiC}} + a_0^I Ix + \left(a_1^{C/\mathrm{SiC}} + a_1^{\mathrm{SiC}} + a_1^I Ix\right)\cos(\phi)\right]^2. \quad (13)$$

Here, x is defined as the distance measured from the cathode to the anode electrode on graphene. The terms $a_0^I Ix$ and $a_1^I Ix$ arise from the current-associated electric field at the graphene/SiC interface, which then produces a FI-SH contribution to enhance surface SHG. Our results of CI-SH measurements at several different graphene locations between the S and D electrodes (data not shown) indicated that the two current-dependent terms are indeed linearly proportional to x. This means that the vertical electric field at the graphene/SiC interface increases linearly with the distance from the cathode to the anode electrode.

From the fit coefficients a_0 and a_1 in Table I, we can solve for the relative values of the three susceptibility tensor elements d_{33}, d_{15}, and d_{31}. Since both a_0 and a_1 are linear functions of these three elements, it seems that in theory a set of values d_{33}, d_{15}, and d_{31} will be uniquely determined from any three of the six tabulated coefficients. However, this is not the case because the $\pm$ sign ambiguity of each a_1 may produce many different sets of possible solutions. In practice, we firstly solve for d_{31} from $a_{1,sp}$ because $a_{1,sp}$ is predominantly determined by d_{31}. We secondly solve for d_{15} from $a_{1,ss}$ because $a_{1,ss}$ is predominantly determined by both d_{15} and d_{31}. Finally, we solve for d_{33} from $a_{0,pp}$ and simultaneously resolve the $\pm$ sign ambiguity by examining the values of the remaining coefficients $a_{1,pp}$, $a_{0,sp}$, $a_{1,ps}$ through a trial-and-error process. Another way to solve for d_{15} is to use the 45°-in/s-out polarization configuration for RA-SH measurements, in which the corresponding fit coefficients a_0 and a_1 are predominantly determined by d_{15}. This allows the amplitude of d_{15} extracted from $a_{1,ss}$ to be cross checked.

The absolute values of d_{33}, d_{15}, and d_{31} can be obtained by calibrating the RA-SH signals from the vicinal-SiC(0001) sample to the RA-SH signals from z-cut quartz [20]. Quartz is used as the reference for SHG because its bandgap is well above the SH photon energy and also because its linear and nonlinear susceptibilities are well known. In particular for the sp polarization, the RA-SH intensity from z-cut quartz is proportional to the square of d_{11} ($\chi^{(2)}_{xxx}$) for quartz, while the RA-SH intensity from vicinal SiC(0001) is proportional to the square of d_{31} for SiC. For quartz, the tensor element $d_{11} = 0.8$ pm/V, the refractive indices $n(\omega) = 1.545$ at 740 nm and $n(2\omega) = 1.569$ at 370 nm [54]. For SiC, the refractive indices $n(\omega) = 2.635$ at 740 nm and $n(2\omega) = 2.840$ at 370 nm [55]. Using these known values and measured SH intensities, we find the tensor element $d_{31} = 18.7$ pm/V for SiC at the SH wavelength of 370 nm. The remaining two tensor elements d_{33} and d_{15} are obtained by calibrating to d_{31}. For the graphene/vicinal-SiC(0001) sample, we include the surface/interface SHG components into the bulk SHG from

TABLE II. Equation (9) fit coefficients $a_{0,pp}$ and $a_{1,pp}$ of the pp-polarized RA-SH scans in Fig. 6 measured from the graphene/vicinal-SiC(0001) sample at three different measurement locations: nearby the S electrode, halfway between S and D, and nearby the D electrode. At each measurement location, three pairs of coefficients respectively correspond to three different current values: no current ($I = 0$), negative current ($I < 0$) at $I = -23$ A/m, and positive current ($I > 0$) at $I = +23$ A/m.

	$I < 0$		$I = 0$		$I > 0$	
Location	$a_{0,pp}$	$a_{1,pp}$	$a_{0,pp}$	$a_{1,pp}$	$a_{0,pp}$	$a_{1,pp}$
Nearby S	−10.82	−4.72	−9.58	−4.31	−9.87	−4.51
Halfway	−10.30	−4.65	−9.57	−4.38	−10.20	−4.69
Nearby D	−9.83	−4.49	−9.59	−4.32	−10.71	−4.79

TABLE III. Measured second-order nonlinear optical susceptibility tensor elements d_{33}, d_{15}, and d_{31} of 6H-SiC at the fundamental wavelength of 740 nm, effective susceptibility tensor elements of surface SHG from the graphene/vicinal-Si(0001) sample, effective susceptibility tensor elements of surface SHG from the current upstream region of the graphene/vicinal-Si(0001) sample when a current of $I = 23$ A/m flows in graphene, and previously reported values of these elements at the fundamental wavelength of 1064 nm.

Sample; wavelength	d_{33} (pm/V)	d_{15} (pm/V)	d_{31} (pm/V)
SiC; 740 nm	−52.0	20.0	18.7
Graphene/SiC; 740 nm	−135.8	18.5	14.6
Graphene/SiC (current upstream region of $I = 23$ A/m); 740 nm	−199.0	18.5	14.6
SiC; 1064 nm, Sato *et al*. (2009) [48]	−12.5	6.5	6.7

the SiC substrate and treat them as a whole piece to obtain a set of effective tensor elements d_{33}, d_{15}, and d_{31} for simplicity. For the graphene/vicinal-SiC(0001) sample without or with current bias in graphene, we summarize the values of d_{33}, d_{15}, and d_{31} in Table III. In extracting the values of these tensor elements, we have removed the contribution of the Fresnel factors (linear optical response) to the SH light.

The measured values of d_{33}, d_{15}, and d_{31} at the fundamental wavelength of 740 nm are ∼3 to 4 times larger than previously reported values of these elements at the fundamental wavelength of 1064 nm [48]. This seems reasonable because stronger nonlinear optical response is expected when the SH light approaches the resonant absorption region of SiC. Our value of $d_{33} = -52$ pm/V of SiC measured at 740 nm, however, nearly agrees on a previously reported value of $d_{33} = -50$ pm/V measured at 1064 nm [52]. In extracting the previous value of $d_{33} = -50$ pm/V at 1064 nm [52], the Kleinman symmetry condition $d_{15} = d_{31}$ was used for simplicity. The condition seems approximately valid, as $d_{15} \approx d_{31}$ for bulk SHG in SiC, but becomes discrepant when surface SHG is significantly involved, as shown in Table III. Some reported values of d_{33}, d_{15}, and d_{31} had been listed in a previous table [48].

The presence of epitaxial graphene leads to a 2.6-times increase of d_{33} but a slight decrease of both d_{15} and d_{31}. The result indicates that the growth of graphene on SiC introduces or strengthens the aligning of vertical bonds at the graphene/SiC interface that are easily hyperpolarized in the surface normal direction. The flow of electric current in graphene leads to additional 1.5-times increase of d_{33} but almost no change to both d_{15} and d_{31}. The result indicates that the vertical electric field that accompanies the current flow in graphene is responsible for enhancement of SHG, while the horizontal electric field, which is much weaker, seems to have a negligible effect on CI-SH.

At the graphene/vicinal-SiC(0001) interface, there should be a buffer layer between pure graphene and the SiC substrate [56–58], which may introduce a SH component with a strength comparable to that from the SiC bulk. The buffer layer includes a carbon interface layer underneath real graphene, which possesses a graphitelike (sp^3 bonded) atomic structure [58] and is covalently bound to the SiC substrate and thus does not behave electronically like graphene. Underneath the carbon interface layer, the buffer layer also includes a layer of Si atoms, which includes Si atoms with dangling bonds and Si atoms with Si-C bonds to link the carbon interface layer. Such a buffer layer does not exist in the graphene/SiO_2/Si(001) sample, and thus no enhancement of SHG is observed on the CVD graphene transferred onto a SiO_2/Si substrate. However, there is probably a transition gap between the transferred CVD graphene and SiO_2, though small enough for van der Waals interactions, to form microcapacitors for charge trapping to build up a vertical electric field for producing FI-SH at the SiO_2/Si interface. In the experiment, the introduction of the buffer layer enhances SHG about 55% on the graphene/vicinal-SiC(0001) sample, while current-associated FI-SH in the buffer layer enhances SHG another 25%. The buffer layer is believed to consist of a combination of sp^2- and sp^3-bonded carbon [56–59], while pure graphene consists of only sp^2-bonded carbon. A strong SH component from the buffer layer but none from graphene suggests that the enhancement of CI-SH from the graphene/vicinal-SiC(0001) sample originates from the sp^3 bonds of carbon in the buffer layer.

The lateral distribution of the vertical electric field for the graphene/SiO_2/Si(001) sample shows a steplike function of the measurement location x in the central graphene region, as shown in Fig. 3(b); however, the vertical electric field for the graphene/vicinal-SiC(0001) sample shows a smooth linear function of x, as indicated by Eq. (13). The difference between the two samples can be understood in terms of charge trapping at the graphene/substrate interface. In the graphene/SiO_2/Si(001) sample, there is a significant amount of structural defects (mostly domain boundaries) between graphene grains to trap negative charges (electrons) and a spatial gap between graphene and SiO_2 to sustain these trapped charges. However, in the graphene/vicinal-SiC(0001) sample, the amount of structural defects in the graphene film is greatly suppressed, and the structural transition from graphene to SiC is continuous. The amount of structural defects in graphene is also expressed by the current density in graphene. For the same voltage we applied, the CVD monolayer graphene on SiO_2/Si can only carry a current density of $I = 2.4$ A/m, but the epitaxial four-layer-graphene film on SiC can carry a significantly larger current density of $I = 23$ A/m, which is still 2.4 times larger if normalized to per monolayer of graphene.

IV. CONCLUSIONS

We have used two millimeter-sized FET-like structures, a graphene/SiO_2/Si(001) structure and a graphene/vicinal-SiC(0001) structure, to study the character and mechanism of CI-SH in graphene. We found that a dc in graphene may enhance surface SHG about three times for a CVD graphene monolayer on a SiO_2/Si substrate, and about 25% for an epitaxial four-layer-graphene film on a SiC substrate. For both the CVD and the epitaxial graphene, we found that the CI-SH signal varies strongly with the measurement location between the source and drain electrodes on current-biased graphene. The location-dependent functions of CI-SH are different for

the two structures: the graphene/SiO_2/Si(001) structure shows a steplike sharp transition, but the graphene/vicinal-SiC(0001) structure shows a smooth transition. Through measurements of FI-SH on the graphene/SiO_2/Si(001) structure, we determined that the CI-SH effect originates from current-associated FI-SH at the SiO_2/Si interface due to charge trapping at the graphene/SiO_2 interface. Through symmetry analysis of CI-SH on the graphene/vicinal-SiC(0001) structure, we determined that the CI-SH effect originates from current-associated FI-SH at the graphene/SiC interface. Our observed variation of CI-SH along the current direction in graphene means that the symmetry breaking caused by current flow in graphene is not the main factor responsible for enhancement of SHG. The similar behavior of CI-SH for both the CVD graphene and the epitaxial graphene in this work suggests that the CI-SH effect in materials is likely due to current-associated electric field-effects. Through RA-SH measurements of the vicinal SiC(0001) substrate, we also determined all three susceptibility tensor elements ($d_{33} = -52.0$ pm/V, $d_{15} = 20.0$ pm/V, and $d_{31} = 18.7$ pm/V) that characterize the second-order nonlinear optical response of hexagonal SiC at the fundamental wavelength of 740 nm. For the graphene/vicinal-SiC(0001) sample, we further determined the three effective susceptibility tensor elements ($d_{33} = -135.8$ pm/V, $d_{15} = 18.5$ pm/V, and $d_{31} = 14.6$ pm/V) for surface SHG, and finally found that the tensor element d_{33} can be enhanced to as large as $d_{33} = -199.0$ pm/V by the flow of a large electric current in epitaxial graphene. We demonstrate that scanning RA-SH is a phase-sensitive probe for characterizing electric current and charge distribution in graphene based devices, and our results of CI-SH suggest a means for combining high electron mobility in graphene with large FI-SH nonlinearity in the graphene/substrate systems to result in new optoelectronic devices.

ACKNOWLEDGMENTS

The authors gratefully acknowledge the Institute for Nanoelectronics Discovery and Exploration (INDEX) and Nanoelectronics Research Initiative (NRI) for partial funding of this work. We thank Chris Bevis of KLA-Tencor for donation of a Tsunami femtosecond laser. We thank Dr. Florence Nelson for growing and transferring of CVD graphene, Dr. Tianhao Zhang for help in constructing the experimental infrastructures for the measurements, Dhiraj Sinha for helpful discussions about charge trapping in CVD graphene, Puneet Suvarna for LabView programming for experimental controls, and Avery Green for critical reading of the manuscript. The vicinal 6*H*-SiC(0001) substrates were purchased from CREE.

[1] K. S. Novoselov, A. K. Geim, S. V. Morozov, D. Jiang, M. I. Katsnelson, I. V. Grigorieva, S. V. Dubonos, and A. A. Firsov, Nature (London) **438**, 197 (2005).
[2] F. Wang, Y. Zhang, C. Tian, C. Girit, A. Zettl, M. Crommie, and Y. R. Shen, Science **320**, 206 (2008).
[3] A. W. Tsen, L. Brown, M. P. Levendorf, F. Ghahari, P. Y. Huang, R. W. Havener, C. S. Ruiz-Vargas, D. A. Muller, P. Kim, and J. Park, Science **336**, 1143 (2012).
[4] A. B. Kuzmenko, E. van Heumen, F. Carbone, and D. van der Marel, Phys. Rev. Lett. **100**, 117401 (2008).
[5] D. Sun, Z.-K. Wu, C. Divin, X. Li, C. Berger, W. A. de Heer, P. N. First, and T. B. Norris, Phys. Rev. Lett. **101**, 157402 (2008).
[6] K. F. Mak, M. Y. Sfeir, Y. Wu, C. H. Lui, J. A. Misewich, and T. F. Heinz, Phys. Rev. Lett. **101**, 196405 (2008).
[7] J. M. Dawlaty, S. Shivaraman, M. Chandrashekhar, F. Rana, and M. G. Spencer, Appl. Phys. Lett. **92**, 042116 (2008).
[8] M. Lewkowicz and B. Rosenstein, Phys. Rev. Lett. **102**, 106802 (2009).
[9] C. H. Lui, K. F. Mak, J. Shan, and T. F. Heinz, Phys. Rev. Lett. **105**, 127404 (2010).
[10] E. Hendry, P. J. Hale, J. Moger, A. K. Savchenko, and S. A. Mikhailov, Phys. Rev. Lett. **105**, 097401 (2010).
[11] X. Yao and A. Belyanin, Phys. Rev. Lett. **108**, 255503 (2012).
[12] H. Yang, X. Feng, Q. Wang, H. Huang, W. Chen, A. T. S. Wee, and W. Ji, Nano Lett. **11**, 2622 (2011).
[13] G. K. Lim, Z. L. Chen, J. Clark, R. G. S. Goh, W. H. Ng, H. W. Tan, R. H. Friend, P. K. H. Ho, and L. L. Chua, Nat. Photonics **5**, 554 (2011).
[14] S.-Y. Hong, J. I. Dadap, N. Petrone, P.-C. Yeh, J. Hone, and R. M. Osgood, Jr., Phys. Rev. X **3**, 021014 (2013).
[15] S. Wu, L. Mao, A. M. Jones, W. Yao, C. Zhang, and X. Xu, Nano Lett. **12**, 2032 (2012).
[16] S. A. Mikhailov, Phys. Rev. B **84**, 045432 (2011).
[17] K. S. Novoselov, A. K. Geim, S. V. Morozov, D. Jiang, Y. Zhang, S. V. Dubonos, I. V. Grigorieva, and A. A. Firsov, Science **306**, 666 (2004).
[18] F. Xia, D. B. Farmer, Y.-m. Lin, and P. Avouris, Nano Lett. **10**, 715 (2010).
[19] M. M. Glazov, JETP Lett. **93**, 366 (2011).
[20] Y. Q. An, R. Carriles, and M. C. Downer, Phys. Rev. B **75**, 241307(R) (2007).
[21] S. A. Mikhailov, Europhys. Lett. **79**, 27002 (2007).
[22] Y. Q. An, J. Price, M. Lei, and M. Downer, Appl. Phys. Lett. **102**, 051602 (2013).
[23] J. J. Dean and H. M. van Driel, Appl. Phys. Lett. **95**, 261910 (2009).
[24] J. J. Dean and H. M. van Driel, Phys. Rev. B **82**, 125411 (2010).
[25] O. A. Aktsipetrov, A. A. Fedyanin, A. V. Melnikov, E. D. Mishina, A. N. Rubtsov, M. H. Anderson, P. T. Wilson, M. ter Beek, X. F. Hu, J. I. Dadap, and M. C. Downer, Phys. Rev. B **60**, 8924 (1999).
[26] A. Y. Bykov, T. V. Murzina, M. G. Rybin, and E. D. Obraztsova, Phys. Rev. B **85**, 121413 (2012).
[27] J. B. Khurgin, Appl. Phys. Lett. **67**, 1113 (1995).
[28] O. A. Aktsipetrov, V. O. Bessonov, A. A. Fedyanin, and V. O. Val'dner, JETP Lett. **89**, 58 (2009).
[29] B. A. Ruzicka, L. K. Werake, G. Xu, J. B. Khurgin, E. Y. Sherman, J. Z. Wu, and H. Zhao, Phys. Rev. Lett. **108**, 077403 (2012).
[30] Y. Q. An, F. Nelson, J. U. Lee, and A. Diebold, Nano Lett. **13**, 2104 (2013).

[31] F. J. Nelson, V. K. Kamineni, T. Zhang, E. S. Comfort, J. U. Lee, and A. C. Diebold, Appl. Phys. Lett. **97**, 253110 (2010).
[32] X. Li, Y. Zhu, W. Cai, M. Borysiak, B. Han, D. Chen, R. D. Piner, L. Colombo, and R. S. Ruoff, Nano Lett. **9**, 4359 (2009).
[33] M. Hupalo, E. H. Conrad, and M. C. Tringides, Phys. Rev. B **80**, 041401 (2009).
[34] C. Berger, Z. Song, T. Li, X. Li, A. Y. Ogbazghi, R. Feng, Z. Dai, A. N. Marchenkov, E. H. Conrad, P. N. First, and W. A. de Heer, J. Phys. Chem. B **108**, 19912 (2004).
[35] Y. Q. An and S. T. Cundiff, Appl. Phys. Lett. **81**, 5174 (2002).
[36] Y. Q. An and S. T. Cundiff, Phys. Rev. B **67**, 193302 (2003).
[37] J. E. Sipe, D. J. Moss, and H. M. van Driel, Phys. Rev. B **35**, 1129 (1987).
[38] Y. Q. An, Ph.D dissertation, University of Colorado at Boulder, 2003.
[39] G. Lüpke, D. J. Bottomley, and H. M. van Driel, J. Opt. Soc. Am. B **11**, 33 (1994).
[40] J. I. Dadap, X. F. Hu, M. H. Anderson, M. C. Downer, J. K. Lowell, and O. A. Aktsipetrov, Phys. Rev. B **53**, R7607 (1996).
[41] Y. Q. An and S. T. Cundiff, J. Appl. Phys. **96**, 2638 (2004).
[42] L. He, J. D. Walker, H. M. Branz, C. T. Rogers, and C. W. Teplin, Appl. Phys. Lett. **101**, 161604 (2012).
[43] Y. G. Lee, C. G. Kang, U. J. Jun, J. J. Kim, H. J. Hwang, H.-J. Chung, S. Seo, R. Choi, and B. H. Lee, Appl. Phys. Lett. **98**, 183508 (2011).
[44] G. Kalon, Y. Jun Shin, V. Giang Truong, A. Kalitsov, and H. Yang, Appl. Phys. Lett. **99**, 083109 (2011).
[45] Y.-J. Kang, J. Kang, and K. J. Chang, Phys. Rev. B **78**, 115404 (2008).
[46] K. Nagashio, T. Yamashita, T. Nishimura, K. Kita, and A. Toriumi, J. Appl. Phys. **110**, 024513 (2011).
[47] S. Niedermeier, H. Schillinger, R. Sauerbrey, B. Adolph, and F. Bechstedt, Appl. Phys. Lett. **75**, 618 (1999).
[48] H. Sato, M. Abe, I. Shoji, J. Suda, and T. Kondo, J. Opt. Soc. Am. B **26**, 1892 (2009).
[49] S. Singh, J. R. Potopowicz, L. G. Van Uitert, and S. H. Wemple, Appl. Phys. Lett. **19**, 53 (1971).
[50] I. J. Wu and G. Y. Guo, Phys. Rev. B **78**, 035447 (2008).
[51] C. Meyer, G. Lüpke, E. Stein Von Kamienski, A. Gölz, and H. Kurz, Appl. Phys. Lett. **69**, 2243 (1996).
[52] P. M. Lundquist, W. P. Lin, G. K. Wong, M. Razeghi, and J. B. Ketterson, Appl. Phys. Lett. **66**, 1883 (1995).
[53] C. Jordan, H. Schillinger, L. Dressler, S. Karmann, W. Richter, K. Goetz, G. Marowsky, and R. Sauerbrey, Appl. Phys. A **65**, 251 (1997).
[54] R. J. Pressley, in *Handbook of Lasers*, edited by R. J. Pressley (Chemical Rubber Company, Cleveland, 1971).
[55] B. Pégourié, Astron. Astrophys. **194**, 335 (1988).
[56] W. A. de Heer, C. Berger, X. Wu, P. N. First, E. H. Conrad, X. Li, T. Li, M. Sprinkle, J. Hass, M. L. Sadowski, M. Potemski, and G. Martinez, Solid State Commun. **143**, 92 (2007).
[57] S. Y. Zhou, G. H. Gweon, A. V. Fedorov, P. N. First, W. A. De Heer, D. H. Lee, F. Guinea, A. H. Castro Neto, and A. Lanzara, Nat. Materials **6**, 770 (2007).
[58] C. Riedl, C. Coletti, and U. Starke, J. Phys. D: Appl. Phys. **43**, 374009 (2010).
[59] F. Nelson, A. Sandin, D. B. Dougherty, D. E. Aspnes, J. E. Rowe, and A. C. Diebold, J. Vac. Sci. Technol. B **30**, 04E106 (2012).